



The Hebrew University of Jerusalem
The Rachel and Selim Benin School of Computer Science and Engineering

Exploring brain region convergence in aging using multiple Quantitative MRI maps

Niv Amos

Thesis submitted in partial fulfillment of the requirements
for the Master of Sciences degree
in Computer Science

Under the supervision of **Prof. Aviv Mezer** and **Prof. Tommy Kaplan**

October 2024

Acknowledgements

First, my deepest gratitude to my two advisors: Prof. Aviv Mezer and Prof. Tommy Kaplan.

Aviv, you taught me with a lot of patience the necessary steps to feel comfortable researching such a complex and amazing organ, the human brain. I've learned so much from you during my time in the lab, and it's been a truly rewarding experience.

Tommy, your tips and lessons have been inspiring for me. Every time we meet, I've learned something new from you, even on topics I thought I already understood. I truly appreciate how you've pushed me to think deeper and grow.

My thanks to my colleagues at the Mezer lab. I have not only gained valuable knowledge from each of you but also forged meaningful and lasting friendships that I will always treasure.

Finally, I want to thank my family for supporting me along the way. For my partner, Amit, thanks for always believing in me and standing by me at every step of the way. Your support has meant everything to me.

Abstract

The human brain undergoes significant changes during aging, affecting both its macrostructure (such as size and shape) and microstructure (the cellular-level properties of brain tissue), impacting its functionality and related to different Neurodegenerative diseases. While previous studies have explored age-related changes in the structure of the human brain and rodent tissues, the relationship between microstructural signatures of in-vivo human brain regions during adulthood remains poorly understood. Here, we investigated the hypotheses that aging leads to the increased similarity of microstructural signatures between different brain regions within an individual, while across different individuals, the microstructural signatures of brain regions show greater variability. For that, we developed a novel qMRI multi-parameter method to create unique microstructural signatures of brain regions. Our analysis of 32 subjects (17 young adults and 15 older adults) using seven different qMRI maps and 128 brain regions for each subject supported both hypotheses: inter-regional microstructural similarity is stronger within older individuals, and the brain regions variability between individuals is greater. Our findings provide new insights into the brain microstructural changes during aging and demonstrate the potential of using multi-parameter qMRI techniques in neuroscience research.

תקציר

המוח האנושי עובר שינויים מסוימים במהלך ההזדקנות, המשפיעים על המבנה המיקרוסקופי שלו (כגון גודל וצורה) והמיקרוסקופי (תכונות רקמת המוח ברמת התא), דבר שמשפיע על תפקודו וקשרו למחלות נוירודגנרטיביות שונות. בעוד שמהקרים קודמים ה证实ו בשינויים הקשורים לגיל במבנה המוח האנושי ובקרמות של מכרסמים, הקשר בין המאפיינים המיקרו-מבנהים של אורי המוח האנושי במהלך הבגרות, נותר מעורפל. במחקר זה בחנו את ההשערות שההזדקנות מובילה לעלייה בדמיהן בין החתימה המיקרוסקופית של אורי מוח שונים בתחום אותו אדם, ומצד שני, מגבירה את השונות בין החתימה המיקרוסקופית של אורי המוח בקרב אנשים שונים. לשם כך, פיתחנו שיטה חדשה מבוססת MRI^q, אשר משתמשת במספר מפות שונות שלכל אחת מהן ערך ביופיזיקלי חשוב אחר, ומטרתה ליוצר חתימה מיקרוסקופית יהודית לכל אורי במוח שבחנו. ניתוח של 32 נבדקים (17 צעירים ו-15 מבוגרים) תוך שימוש בשבע מפות MRI^q וב-128 אורי מוח עבר כל נבדק, מצאנו תמיכה בשתי ההשערות: הדמיון המיקרוסקופי בין אורי מוח שונים בתחום אותו נבדק חזק יותר אצל אנשים מבוגרים יותר, והשונות בין הנבדקים המבוגרים גם כן גדולה יותר. הממצאים שלנו מספקים תובנות חדשות בנוגע לשינויים המיקרו-מבנהים במוח במהלך ההזדקנות ומדגימים את הפוטנציאלי של טכניקות MRI^q מרובות פרמטרים במחקר מדעי המוח.

Contents

1	Introduction	1
2	Background	4
2.1	Magnetic Resonance Imaging (MRI)	4
2.2	Quantitative MRI (qMRI)	5
2.2.1	Relaxation	5
2.2.2	Magnetization Transfer (MT)	6
2.2.3	Macromolecular Tissue Volume (MTV)	6
2.2.4	Diffusion	7
3	Results	8
3.1	Dataset construction and preprocessing for microstructural signature analysis	8
3.2	Analytical tests to validate the reliability of the qMRI vector	11
3.2.1	Binary classification of ROIs	11
3.2.2	Neuroanatomical areas clustering	13
3.2.3	Similarity between homologous cortical brain regions	16
3.3	Brain regions microstructure signature similarity during aging	17
3.4	Microstructure signature similarity across individuals with aging	21

Discussion	23
4 Methods	26
4.1 Overview	26
4.2 Subjects	26
4.3 MRI acquisition	26
4.4 Estimation of qMRI parameters	27
4.5 Brain segmentation	27
4.6 Dataset construction	28
4.7 Outliers handling	28
4.8 Correlations analysis	29
4.9 Statistical significance	29
4.10 Dimensionality reduction using t-SNE	30
4.11 XGboost model for Binary Classification	30
References	30

1 Introduction

Aging is a complex biological process. During aging, numerous changes take place in humans, affecting various domains - from appearance and behavior to the structure and function of tissues and cells (Harman, 1981). Aging is also accompanied by changes in the brain, contributing to structural and functional impairments in cells, tissues, and blood vessels (Peters, 2006) and in macrostructural organization (Fjell and Walhovd, 2010; Lockhart and DeCarli, 2014). Aging is also related to multiple Neurodegenerative brain diseases (Dugger and Dickson, 2017; Hung et al., 2010; Hou et al., 2019).

The brain is made of multiple distinct regions each with its own function and therefore its unique cellular organization and molecular signature. An interesting observation related to aging suggests that areas that are distinct in their molecular signatures in adulthood become less distinct due to the aging process. This was observed using RNA expression in different body organs including rodent cortex (Izgi et al., 2022). While this phenomenon has been studied *ex vivo* on rodent several cortical regions, its presence and impact on the human brain *in vivo* remain unclear (as illustrated in Fig. 1.1 x-axis).

One of the primary non-invasive techniques used to map the aging process in the human brain is Magnetic resonance imaging (MRI) (Peters, 2006; Fjell and Walhovd, 2010; Lockhart and DeCarli, 2014; Sowell et al., 2004; Raz et al., 2005). MRI uses a strong magnetic field to visualize the brain's structure by exploiting the magnetic properties of hydrogen atoms in water molecules. Advances in the field have led to the development of quantitative MRI (qMRI). This technique provides biophysical microstructural sensitive parametric measurements of the human brain. For further details about MRI and qMRI imaging techniques, see Background below.

Such MRI and qMRI are shown to be a suitable tool to track age-associated

changes *in vivo* and be shown to be very useful for investigating and diagnosing various aging processes (Callaghan et al., 2014; Yeatman et al., 2014; Gracié et al., 2017; Carey et al., 2018; Filo et al., 2019). An important open question is how these multiple microstructural parameters are interrelated and how they change relative to each other as a function of age.

Cortical thickness is a measurement of the thickness of the outer layer of the brain, known as the cortex, and it has been proven to be a reliable indicator of the aging process (Thambisetty et al., 2010; Burzynska et al., 2012). Paquola et al. (2019b,a) estimated cortical thickness from microstructural qMRI data (magnetization transfer, MT), showing that it can co-vary across the brain as a measure of how similar certain brain regions are within an individual. Nevertheless, these studies have not examined how these brain patterns of similarity related to the convergence of various brain regions, and whether they manifest as an increase in similar pattern levels during aging.

Nadig et al. (2021) proposed that cortical aging is a unique process for each individual, resulting in the aged cortex of one person being less similar to those of other age-matched, old adults. While this finding has been shown in the cortex using cortical thickness, it remains uncertain whether this pattern applies to other brain regions and other MRI-based microstructural measurements (as shown on the y-axis in Fig. 1.1).

Here, we present a novel qMRI analysis method to test the convergence of brain regions during aging, by using a multi-parametric approach that leverages the combined assessment of multiple quantitative imaging biomarkers across multiple cortical and non-cortical brain regions. We used an qMRI dataset, containing 32 young and older adult subjects. For each subject, we used seven qMRI maps representing different microstructure measures: R1, T2, MTV, MT, R2*, Diffusion FA, and Diffusion MD (see Background for the details about those parameters). Specifically, we examined two hypotheses. First, whether within an individual brain, the microstructural signatures of different regions, are distinct in young adults and become increasingly similar with age. Second, we test the hypothesis that the similarity of these microstructural signatures across different individuals is reduced with age. Fig. 1.1 illustrates these hypotheses. We also tested our method with several analytical tests, that approved its credibility and usage.

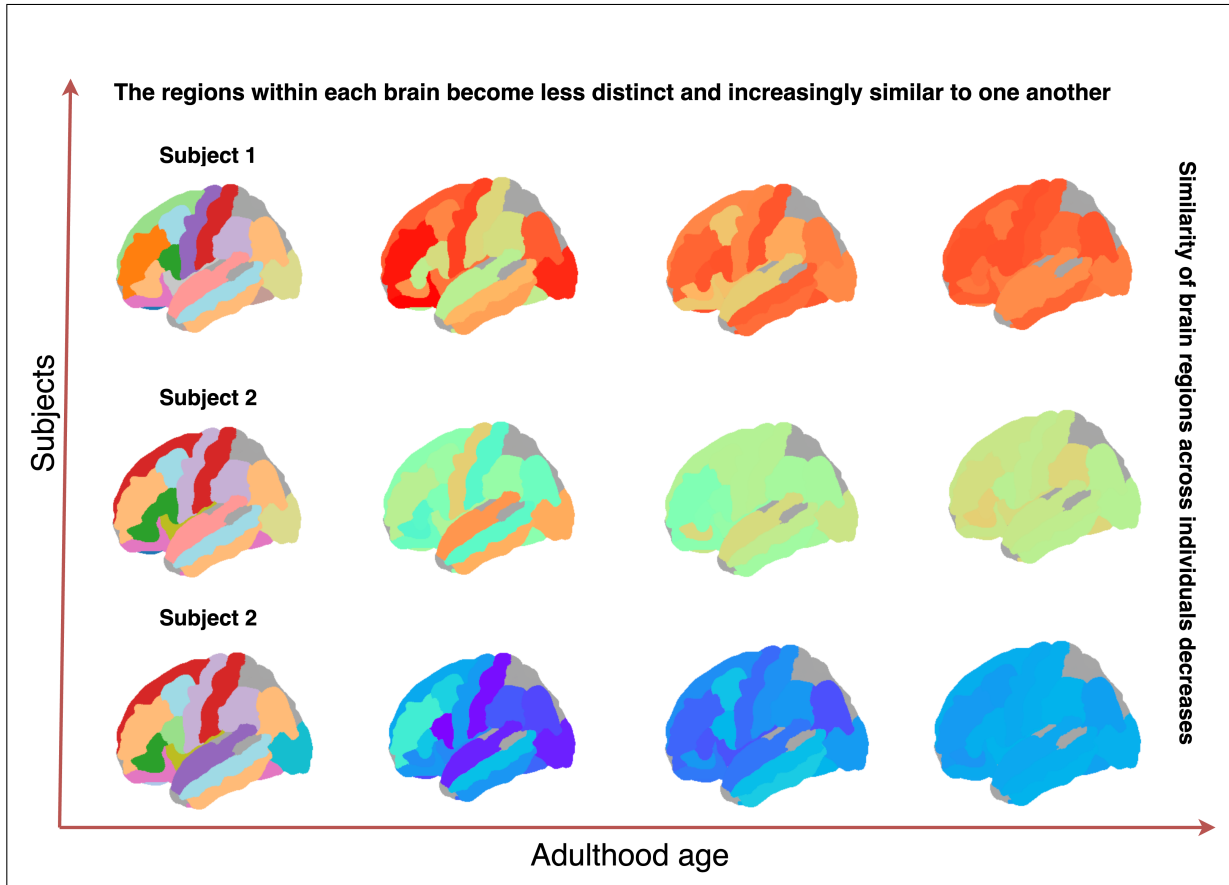


Figure 1.1: An illustration of our hypotheses. From left to right, the figure shows the progression of adulthood aging: initially, the brain regions exhibit distinct characteristics (represented by different colors). From top to bottom, the figure represents different individuals' brains, where these regions appear relatively similar at an early age. As aging progresses, the regions within each brain converge toward similar expression levels, becoming less distinct (with similar colors, representing similar values), while the similarity of these regions across different individuals decreases.

2 Background

This chapter discusses the concepts and foundational principles relevant to understanding the imaging techniques used in this study.

2.1 Magnetic Resonance Imaging (MRI)

MRI is a non-invasive imaging technique widely used in medical diagnostics and research (Morrow et al., 2011; Frisoni et al., 2010; Chougar et al., 2020) to visualize the structure and function of the body's organs, particularly the brain. MRI works by exploiting the magnetic properties of atomic nuclei, primarily hydrogen atoms in water, which are plentiful in biological tissues, especially in the brain.

When a person is placed in a strong magnetic field, such as that used in MRI machines, the magnetic vector of protons in the hydrogen nuclei (primarily in water) aligns with the field direction, known as the Z-axis. By applying radiofrequency (RF) pulses, the protons are temporarily disturbed from their alignment and flipped to the XY plane (transverse plane). The angle at which the protons are flipped depends on the strength and duration of the RF pulse. Once the RF pulse is turned off, the protons gradually return to their original alignment (Z-axis). This rotating magnetic field generates an electrical current in the receiver, which can be detected by the MRI scanner. The electric signal over time is encoded in 2D Fourier space, allowing the detailed images of the body's internal structures to be reconstructed. These images are referred to as T1-weighted, T2-weighted, or proton-density-weighted (PD) images, depending on the contrast mechanism used. See (Hashemi et al., 2012; Plewes and Kucharczyk, 2012) for further information.

MRI is particularly useful for brain imaging (Dugger and Dickson, 2017; Vernooij et al., 2007; Bauer et al., 2013; Lockhart and DeCarli, 2014), as it provides excellent contrast between soft tissues. Traditional MRI, however, typically provides qualitative images, meaning that while it offers visual details, it doesn't necessarily quantify the underlying tissue properties that could offer deeper insights into physiological or pathological states.

2.2 Quantitative MRI (qMRI)

Weighted images are used to detect contrast changes that can be observed by the human eye or computer vision. It is composed of multiple voxels and by definition used for macroscale measurements, such as detecting lesions, strokes, tumors, and other abnormalities (Guo et al., 2015; Zhang et al., 2021; Leung et al., 2014). Advancements in MRI technology led to the development of Quantitative MRI (qMRI). qMRI uses multiple weighted images to fit a signal equation and assign a physical value to each voxel. These values reflect the underlying biophysical properties of the tissue, enabling more precise assessments of microstructural changes that are not detectable with standard weighted imaging techniques.

In this study, we used several quantitative parameters. These parameters are essential for characterizing tissue structure at a microscopic level. Each of these parameters offers distinct insights into tissue composition and behavior:

2.2.1 Relaxation

Relaxation in MRI is the process that occurs after the radiofrequency pulse is transmitted, where protons return to thermal equilibrium with their environment. This involves two key processes: (1) the recovery of longitudinal magnetization along the Z-axis (T1 relaxation), and (2) the decay of transverse magnetization in the XY plane (T2 and T2* relaxation). These processes follow exponential patterns and are characterized by specific time constants: T1, T2, and T2*.

T1 Relaxation (Longitudinal Relaxation)

T1 is the time (in milliseconds) it takes for the longitudinal magnetization (along the Z-axis) to realign with the direction of the Z-axis after the radio frequency pulse disrupts it. This measurement is sensitive to interactions between water molecules and paramagnetic regions (Edwards et al., 2018).

T2 and T2* Relaxation (transverse relaxation times)

T2 is the time (in milliseconds) it takes for the magnetization in the XY plane to decay after the radiofrequency pulse is applied. This decay happens because nearby protons interact and lose their synchronized spinning, leading to signal loss over time. T2* relaxation describes a similar process but also includes additional signal decay caused by small variations in the magnetic field strength and differences in tissue composition, making T2* decay faster than T2. Both T2 and T2* are sensitive to the local magnetic environment, including interactions with paramagnetic and diamagnetic tissue components like iron (Edwards et al., 2018).

From these measurements, the relaxation rate (R_1 , R_2 , and R_{2^*}) can also be calculated, which is the inverse of T1, T2, and T2*, respectively.

2.2.2 Magnetization Transfer (MT)

In Magnetization Transfer (MT) we excite protons in macromolecules, and the signal from the excited macromolecule protons is transferred to nearby water molecules. As a result, some of the water molecules can not be seen, because their signals are already excited and thus reduced. By analyzing this reduction, we can estimate the fraction of macromolecules and the rate at which the magnetization is transferred from macromolecules to free water.

2.2.3 Macromolecular Tissue Volume (MTV)

Macromolecular Tissue Volume (MTV) measures the non-water content in each voxel, with the remaining volume representing water. The water content is estimated from the Proton Density (PD) signal, which is propor-

tional to the amount of water in the voxel. The water volume fraction is calculated from the PD signal, and MTV is defined as **1 minus water fraction**, representing the non-water content in the tissue. The slope, or rate of change in relaxation, is sensitive to the non-water fraction and the tissue's molecular structure, revealing how the tissue affects relaxation and providing insights into its microstructure (Mezer et al., 2013).

2.2.4 Diffusion

The cell membrane layers and myelin sheaths on the neuronal fibers inhibit and slow the diffusion of water molecules. Due to the anisotropic (direction-dependent) properties of the fibers and their anisotropic orientation distribution, water diffusion in the cortex is also anisotropic. Diffusion is measured using diffusion MRI (dMRI), which tracks the movement of water molecules by applying a series of gradient pulses in different directions. The degree to which water molecules diffuse is then quantified, typically through metrics like **Fractional Anisotropy (FA)** and **Mean Diffusivity (MD)**. These measurements provide information about neuronal fibers (particularly axons and dendrites), which act as barriers and inhibitors to water diffusion on a microstructural level. Some of the information that can be inferred from the anisotropy in diffusion includes the orientation distribution of the fibers (Anderson, 2005).

3 Results

3.1 Dataset construction and preprocessing for microstructural signature analysis

To explore the relationship between the microstructure signature of the brain and age, we propose a novel usage of a multi-parameter qMRI vector, representing the microstructure signature for each selected brain region. Specifically, we tested two hypotheses. First, inside one's brain, different regions microstructure signatures are distinct in the young and become more similar with aging. Second, during aging the microstructure signature similarity between individuals is reduced.

To test these hypotheses we constructed our dataset through the following steps: We used 32 young and older adult subjects. For each of them, we used seven qMRI maps described previously. From each of these maps, we extracted data (voxel values) from 128 distinct brain regions of interest (ROI). The ROIs were selected from different neuroanatomical areas, from both hemispheres, areas such as cortical, white-matter, and sub-cortical regions using FreeSurfer's (Fischl, 2012) automated cortical parcellation method (Desikan et al., 2006). We then standardized the values within each map by calculating z-scores (based on values from the entire regions), addressing the differing scales across the maps. To further enhance data robustness and reduce computation time, as each map contains tens of thousands of voxels and values, we computed the median value for each region across the 7 qMRI maps. Thus, for each subject, we obtained a 128×7 matrix where each row is a region, represented by a 7-value vector, with each value corresponding to the median of the qMRI values for that region - we call this vector the region **signature**. Additionally, we

removed noisy outliers from the data, as these subjects were suspected of non-microstructural sources such as movement during the scan. For a visual representation of the preprocessing steps, see Figure 3.1.

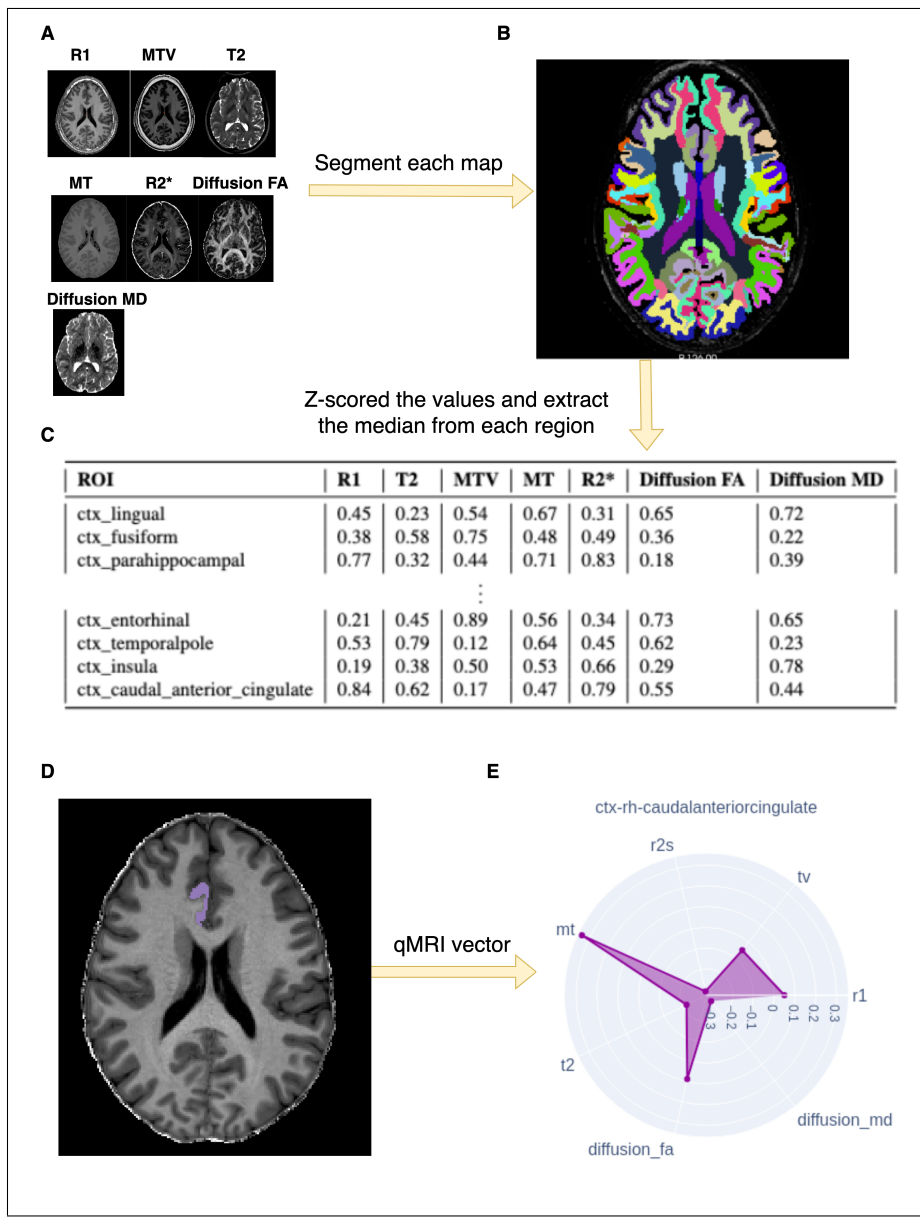


Figure 3.1: Illustration of our preprocessing method for a single subject. **A.** Visualization of the qMRI maps. **B.** Extraction of brain regions from each map using the Freesurfer automated parcellation method. **C.** Z-scoring of values from each map, followed by the extraction of the median value for each region to construct a 128×7 matrix representing the subject's brain regions. **D.** An example of a cortical region processed with our method. This region is represented by a 7-value median vector, displayed using a polar plot that characterizes its unique signature.

3.2 Analytical tests to validate the reliability of the qMRI vector

Before using the multi-parameter qMRI vector to investigate the relationship between brain microstructure properties and age, we first demonstrate its robustness and reliability as a brain measure. Therefore, we have conducted a series of analytical tests to validate its effectiveness.

3.2.1 Binary classification of ROIs

This experiment aimed to determine whether using a multi-parameter qMRI vector enhances the accuracy of classifying age groups for each ROI, and how it can be compared to a single-parameter approach. To this end, we employed the XGBoost classification algorithm, a powerful gradient-boosting framework that excels at handling structured data (Wu et al., 2021) by building an ensemble of decision trees to improve classification accuracy.

The goal was to assess whether each ROI signature corresponds to its respective age group (young or old). First, the dataset was split into training and testing sets, with 80% allocated for training the model and 20% for testing it. We stratify the training data with all of the different ROIs, to make sure the training process represented all of the regions.

Then, we trained a model with all the seven qMRI parameters, and also seven more models, each trained only with one of the qMRI parameters' median values. Finally, the multi-parameter and single-parameter models were tested to compare their effectiveness.

The multi-parameter model demonstrated significantly better performance, achieving a precision of $\sim 90\%$, as shown in Table 3.1, while none of the single-parameter models surpassed 68% - MTV model has achieved the higher precision from those single-parameter models. This outcome underscores the advantage of using multiple parameters for accurately classifying ROIs by age group. The most influential features in the classification were MTV and R1, as measured by gain — a metric that quantifies the average improvement in accuracy when a feature is used for a split in the decision trees. Features with higher gain contribute more to the overall predictive power of the model, illustrated in Figure 3.2.

Table 3.1: Binary classification evaluation matrix on young and old subjects using XGBoost, comparing the usage of a multi-parameter vector versus individual qMRI maps.

Metric	Multi-parameter	R1	T2	MTV	MT	R2*	Diffusion FA	Diffusion MD
Precision ($\frac{TP}{TP+FP}$)	91%	52%	60%	67%	53%	59%	52%	59%
Recall ($\frac{TP}{TP+FN}$)	91%	52%	59%	67%	53%	59%	52%	58%
F1-Score ($2 \times \frac{\text{Precision} \times \text{Recall}}{\text{Precision} + \text{Recall}}$)	91%	51%	58%	67%	52%	59%	52%	58%

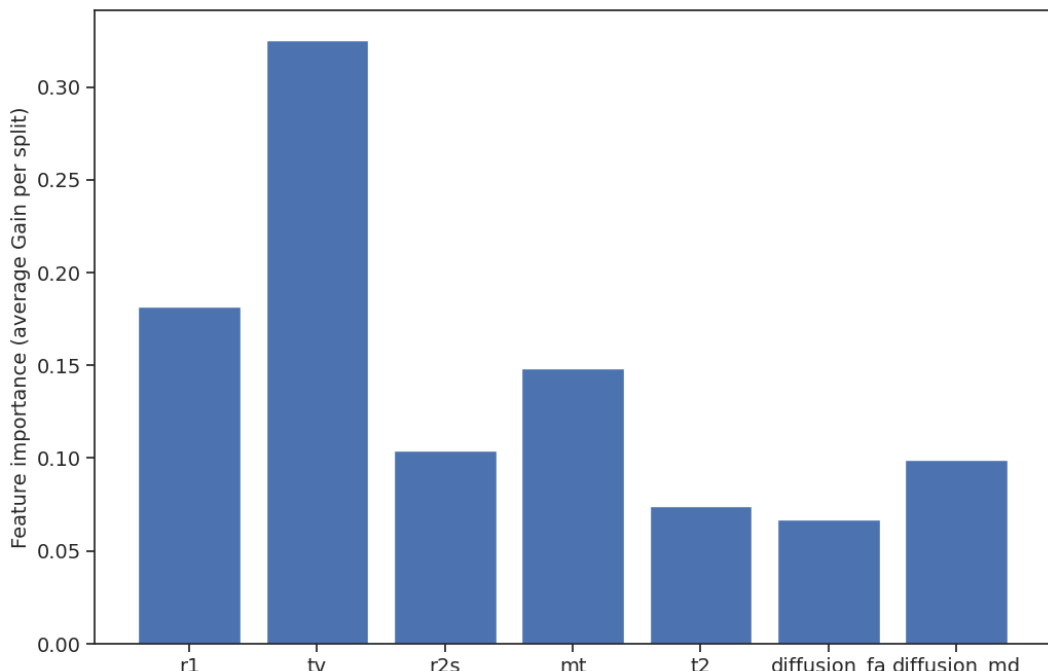


Figure 3.2: Features importance for the binary classification of young and old ROIs

3.2.2 Neuroanatomical areas clustering

To evaluate whether our method yields meaningful representations of the ROI signature, we employed t-SNE (t-distributed Stochastic Neighbor Embedding) model, which is a non-linear dimensionality reduction technique that projects high-dimensional data into a lower-dimensional space, to visualize how these regions group according to their neuroanatomical categories (cortical, white matter, subcortical). t-SNE is particularly useful for revealing local structures in the data by preserving the relationships between neighboring data points. We included all ROIs (each shaped as 1×7) from all subjects in our study.

Before applying t-SNE, we performed principal component analysis (PCA) to reduce the dimensionality while retaining 95% of the variance. This step was essential, t-SNE tends to work better on lower-dimensional data because it can be computationally expensive and sensitive to noise in high-dimensional spaces. The cumulative explained variance plot, shown in Fig. 3.3, demonstrates how many principal components were needed to retain 95% of the variance.

After dimensionality reduction, we applied t-SNE to project the data into 2D for visualization. As illustrated in Fig. 3.4, the model effectively differentiated between neuroanatomical areas with notable clarity, indicating that our approach retains the distinctive neuroanatomical features of the ROIs. Additionally, we filtered the subcortical regions from the clustering to highlight the internal subcortical clusters.

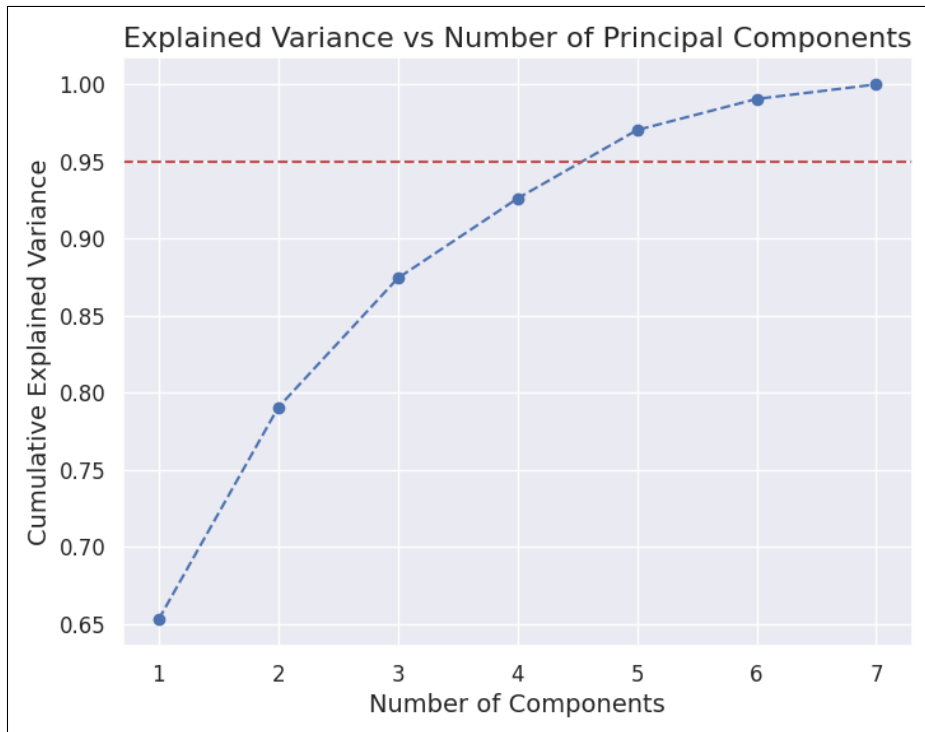


Figure 3.3: Cumulative explained variance plot from Principal Component Analysis (PCA) applied to the ROIs data. The plot shows how many principal components were needed to retain 95% of the variance, helping to reduce dimensionality while preserving the most important information.

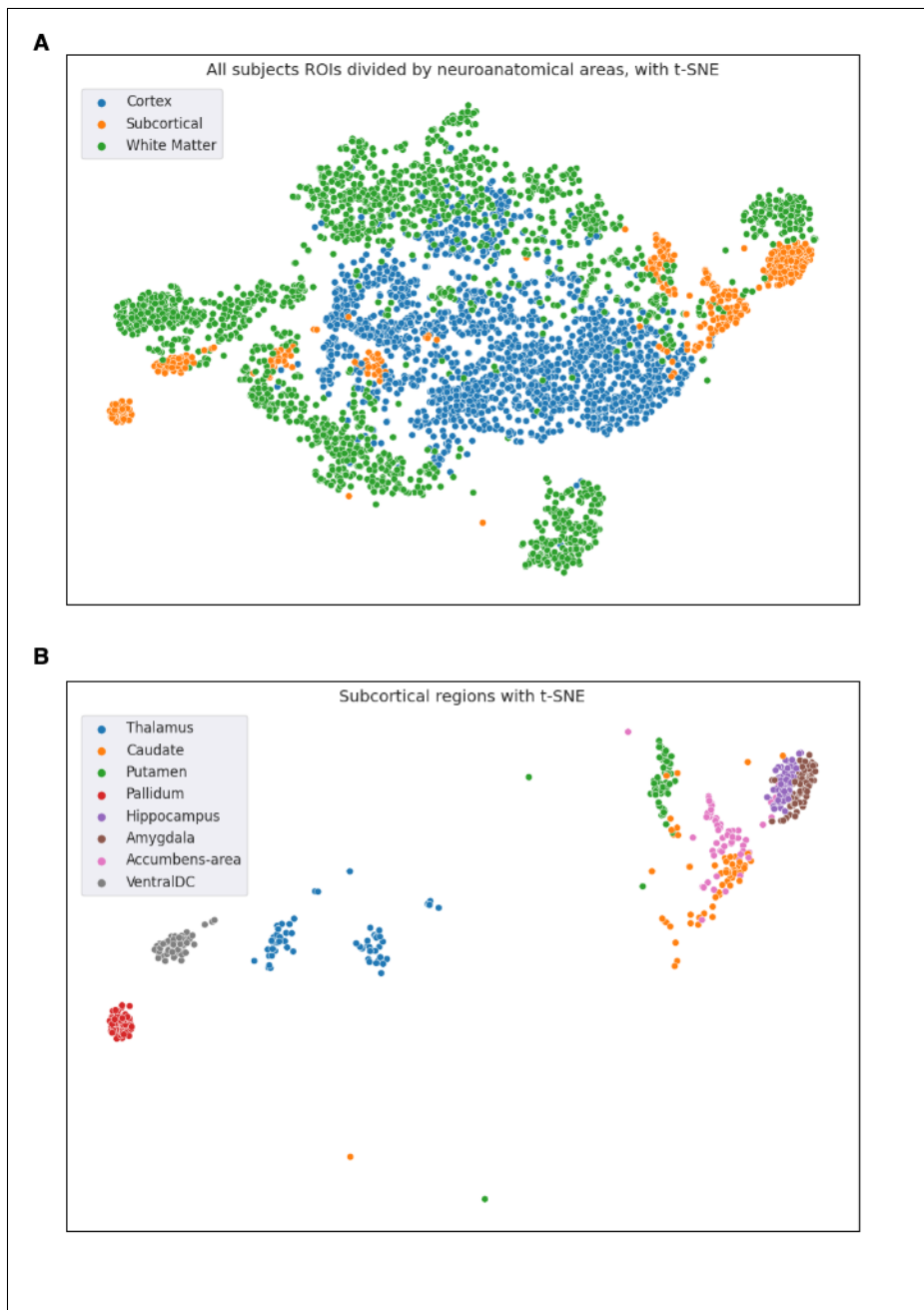


Figure 3.4: t-SNE visualization of ROI representations after dimensionality reduction. All regions of interest (ROIs) from every subject, initially reduced via PCA to retain over 95% of the variance, were further projected into two dimensions using t-distributed Stochastic Neighbor Embedding (t-SNE). **A.** The resulting clusters are color-coded by neuroanatomical categories - cortical, white matter, and subcortical. **B.** Filtering the subcortical regions from **A**, to show the inner clusters.

3.2.3 Similarity between homologous cortical brain regions

As a measure of reliability, we examined whether the similarities between signatures of homologous cortical brain regions - i.e., the same regions from the left and right hemispheres - were greater than those between non-homologous cortical regions (Fig. 3.5). To achieve this, we computed the cosine similarity between the qMRI median vectors of each region, producing a 52×52 (as the number of cortical regions) similarity matrix per subject. These matrices were averaged across all subjects to generate a mean similarity matrix. By comparing the collective mean similarity of homologous regions to that of non-homologous regions, we observed that homologous regions, on average, exhibited significantly higher similarity.

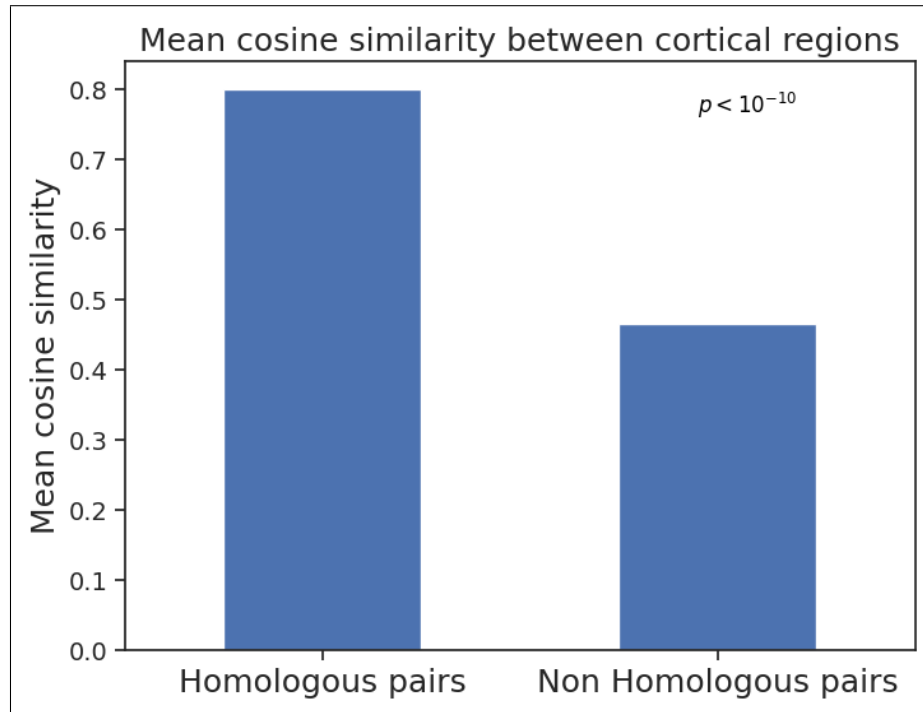


Figure 3.5: The mean cosine similarity between homologous and non-homologous cortical brain regions. The homologous regions have significantly higher similarity on average.

3.3 Brain regions microstructure signature similarity during aging

After establishing our microstructure signature approach, we continued to investigate our hypothesis that the microstructure signatures of brain regions are distinct in young individuals and become more similar with age. We examined the inter-regional correlations among subjects and assessed the impact of aging. We specifically analyzed the correlations between regions of interest (ROIs) across all neuroanatomical areas, for both age groups. Our analysis proceeded as follows:

Initially, to establish a baseline for further analysis, we computed the cosine distances between the ROI vectors for each subject and averaged these distances across the entire dataset. We then performed hierarchical clustering on the ROIs using these average distances. The resulting cluster order was preserved for subsequent steps in our analysis, and to highlight the correlations of the regions that were clustered together.

Next, we calculated the Pearson correlation coefficients between the ROI vectors for each subject, generating a correlation heatmap matrix. To assess the overall correlation patterns within each age group, we then averaged these correlation coefficients across all subjects in each group, resulting in an average correlation matrix for both the young and old groups.

To identify the correlation patterns of each group, we calculated the mean value of each region's correlation vector, derived from each row of the average correlation matrix. This mean value represents the average correlation strength of each region with all other regions, thereby highlighting the most connected areas of the brain.

We performed an independent two-sample t-test to compare the overall average inter-regional correlations between the brain regions of older and younger subjects, identifying a significant difference between the groups ($p < 0.001$). Specifically, older subjects demonstrated higher inter-regional correlations than younger subjects across almost all of our tested brain regions.

When analyzing the average correlations within each neuroanatomical area separately (comparing the average correlations only between brain regions within each specific area), we found that the correlations in the cortex of older subjects differed significantly from those of younger subjects ($p <$

10^{-8}), with nearly all regions showing higher correlations in the older group. However, for other neuroanatomical areas, such as white matter and subcortical regions, there was no notable difference between the groups, $p > 0.6$ for white matter and $p > 0.4$ for subcortical. For each neuroanatomical area, we used an independent two-sample t-test between the two groups, to check for significant differences.

These findings are illustrated in Fig. 3.6, which also displays a cortical surface plot generated using Nilearn (Abraham et al., 2014). This visualization highlights the differences in the inter-regional average correlations between the two age groups, providing a comprehensive overview of the changes in brain connectivity with aging. In Fig. 3.7 we can see an example of the differences between two cortical regions, showing how the region's signatures on the adult subjects overlap more on average.

To validate our findings, we conducted a bootstrap analysis by resampling subjects with replacement over 1,000 iterations. For each resampled dataset, we repeated the same steps as described above, and ended up with the mean value of each region's correlation vector for both the young and old groups. This resulted in 1,000 lists of mean correlation values from each brain region, for each group. We then averaged these lists across all iterations for both groups.

For each brain region, we calculated the 95% confidence intervals of the mean correlation values based on these bootstrap samples. These confidence intervals represent the range within which the true mean correlation value for each region is likely to fall, with 95% confidence, based on the resampled data. All the original observed average correlation values were within these intervals, confirming the higher inter-regional correlations in older subjects and validating the stability of our results across iterations.

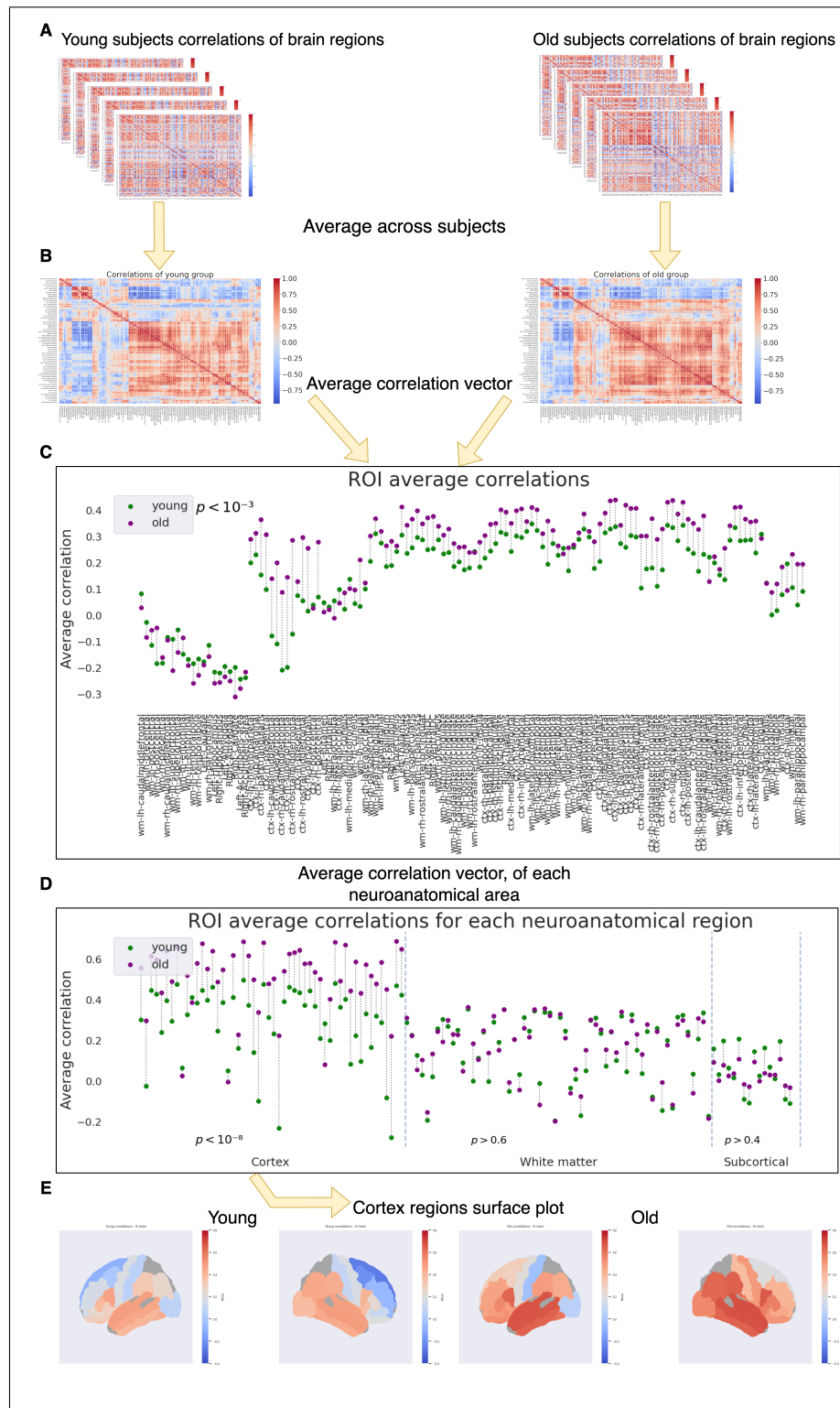


Figure 3.6: Overview of our ROIs correlations analysis. **A.** Correlation matrices were created for each subject in both age groups, representing the correlations between all ROIs. **B.** We averaged these correlation matrices within each age group to produce a mean correlation matrix. **C.** For each ROI, the mean value of its correlation vector (each row in the average correlation matrix) was calculated to assess overall correlation strength. The results show that brain regions in older subjects are generally more correlated than in younger subjects. **D.** This step was repeated for regions within each neuroanatomical area separately, revealing that cortical regions exhibit significantly higher correlations in older subjects than younger ones. **E.** To visualize these findings, we mapped the average correlations for each cortical region onto a cortical surface, highlighting the increased connectivity in older subjects.

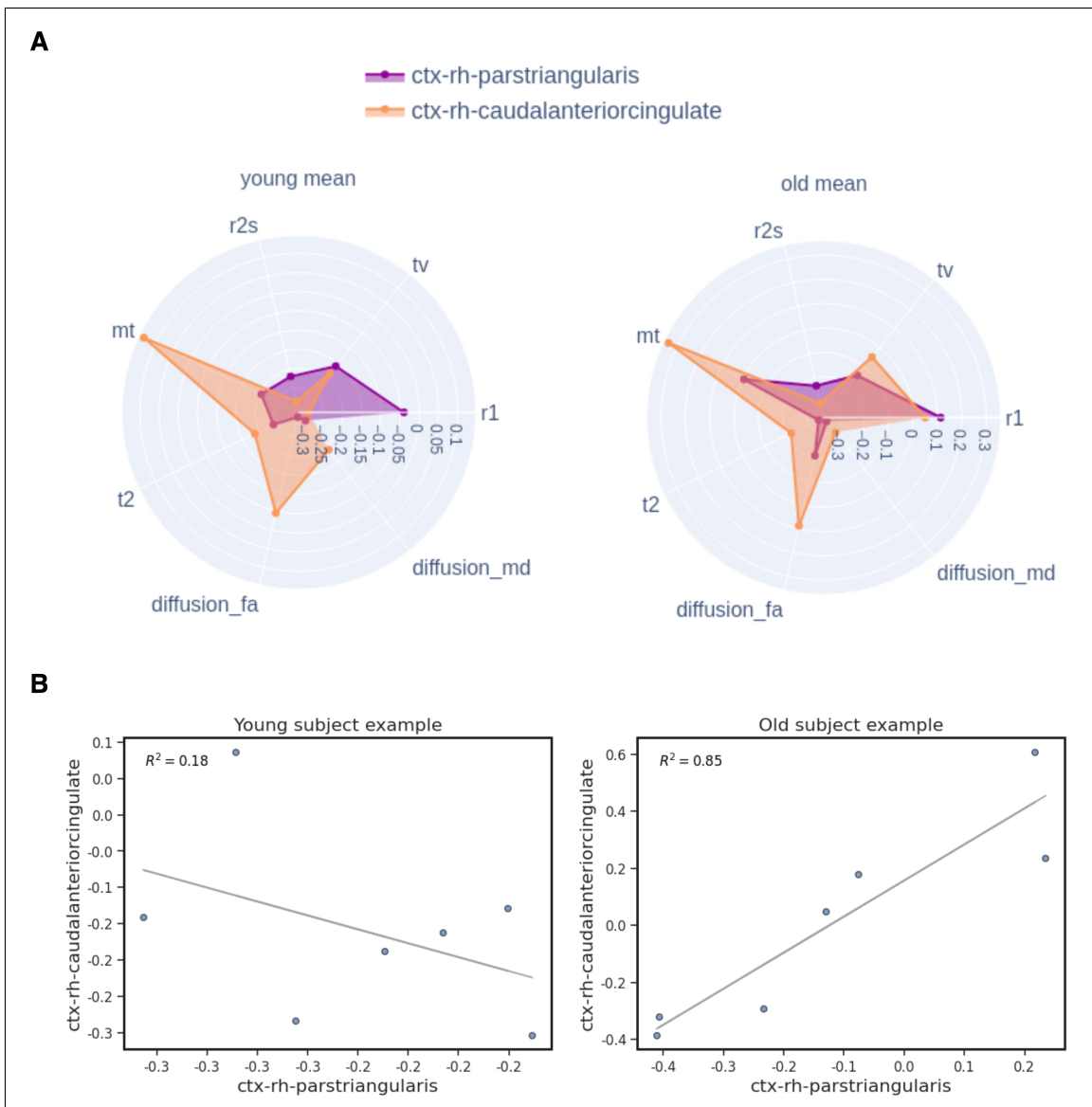


Figure 3.7: Comparison of two cortical regions: right caudal anterior cingulate and right pars triangularis. **A.** Mean values from the median qMRI vector for both regions were calculated and visualized using a polar plot for each age group, showing greater overlap in older subjects, indicating increased similarity. **B.** A linear regression model was applied to the vectors from both regions for a random example subject from each age group. The model fit the vectors from these regions significantly better in older subject, with an R^2 value of 0.85 compared to 0.18 in younger subject , indicating a stronger relationship between these regions in older individuals.

3.4 Microstructure signature similarity across individuals with aging

To assess our second hypothesis, that during aging the microstructure signature similarity across individuals decreases, we calculated the standard deviation of each region's qMRI vector values across all subjects in each age group, averaging these values for each parameter. Our analysis revealed that in most regions, older subjects exhibited greater variability across all neuroanatomical regions (Fig. 3.8). Notably, the subcortical regions, showed the largest difference in variability between the older and younger groups, indicating that these regions are more disrupted in older individuals.

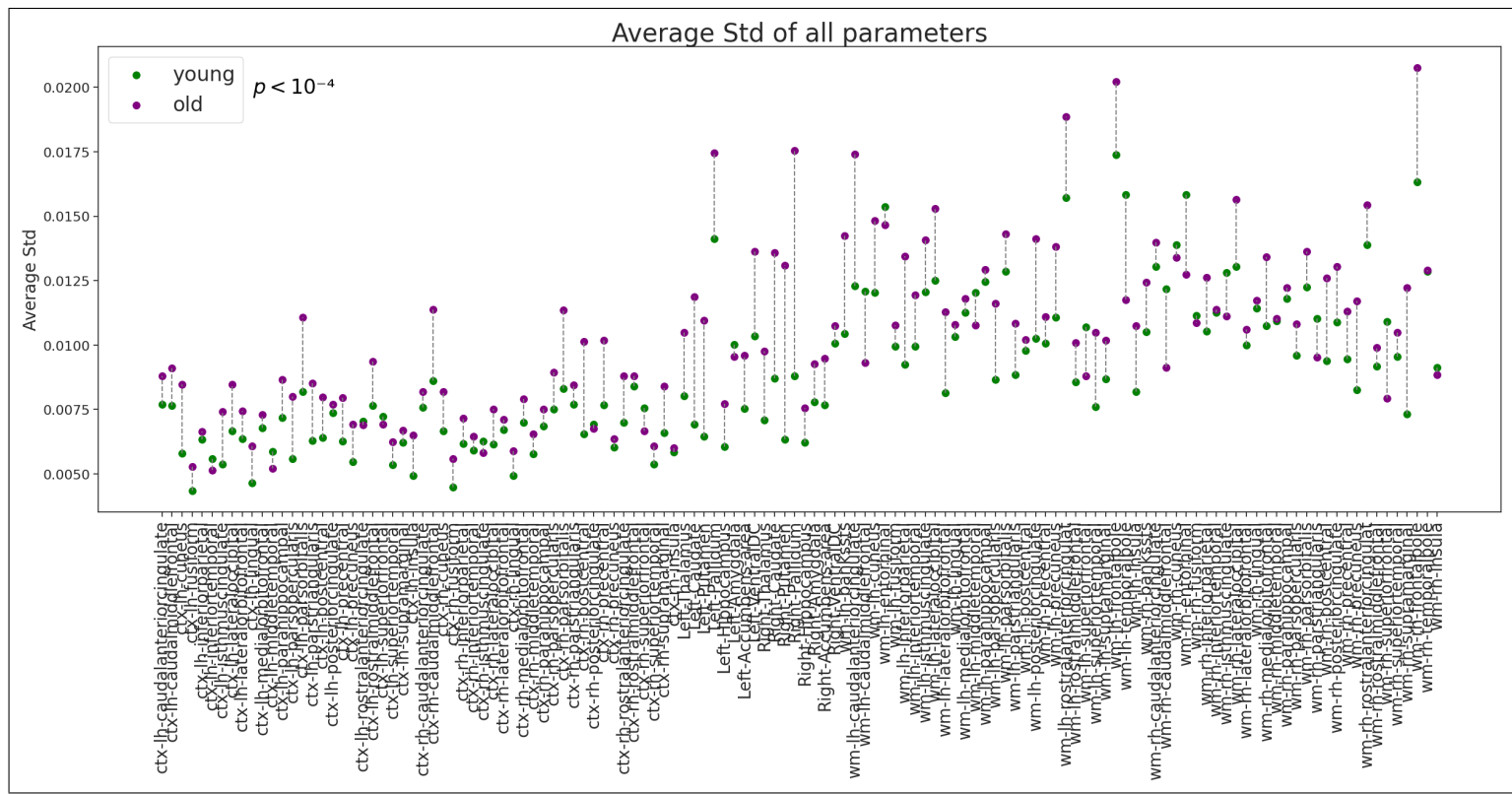


Figure 3.8: Variability of brain regions across age groups. The scatter plot compares the average standard deviations of qMRI vectors for each brain region between young and old subjects. Each point represents a specific region, with greater variability observed in older subjects across most regions. Notably, subcortical regions showed the largest differences in variability, indicating increased disruption in these areas within the older group.

Discussion

Our study utilized qMRI dataset to investigate the microstructural changes in the brain associated with aging. We developed a novel multi-parametric method to analyze a multi-dimensional dataset. Using this approach, we tested two hypotheses regarding the similarities between brain regions microstructure signatures, within or between individuals. Our findings provide new insights into the adulthood aging process of the human brain and support our initial hypotheses.

Firstly, we showed that microstructural signature similarities between different brain regions increase with age, especially in the cortical regions. This finding may suggest that aging is associated with a loss of regional specificity, since the microstructural values of the aged brain tend to converge, resulting in a more homogeneous brain. This result agrees with previous studies in post-mortem gene expression in the rodent cortex and other body regions (Izgi et al., 2022). In those studies, it was hypothesized that tissues converge during aging due to the loss of tissue identity. It is interesting to consider that a similar process also affects the MRI microstructural signature.

Secondly, we analyzed the standard deviation of qMRI vector values across subjects in each age group. In this analysis, we support the hypothesis, that the similarity of microstructural signatures of brain regions across different individuals decreases with age. Previous work by (Nadig et al., 2021) showed that anatomical imbalance, which measures deviations from typical brain structure patterns, decreases during development but increases with aging, suggesting that brain morphology becomes more individualized with age. In agreement, we found greater variability in older subjects across most brain regions. It suggests that as individuals age, each brain uniquely changes. One can speculate several possible sources for such differences between individuals that include genetics (Kremen et al.,

2010; Izgi et al., 2022), lifestyle factors (Erickson et al., 2011; Valls-Pedret et al., 2015), environmental exposures (Kremen et al., 2010) or medical history (Wrigglesworth et al., 2023; Muller et al., 2014).

In this work, we devised a new approach to asses a multi-parametric vector of microstructural signature. Therefore we also try to assess this vector approach usefulness and robustness. First, we showed that this approach allows a classification of the age group of each of the brain regions' microstructural signatures. By using a multi-parameter approach, one may get up to 20% improvement in precision compared to a single-parameter approach. This is a notable gap, which shows the added value of integrating multiple qMRI biomarkers to capture the complex nature of brain aging. Importantly predicting the biological age of the brain and its sub-regions is a rising field of research with great clinical potential (Baecker et al., 2021; Lee et al., 2022; Aycheh et al., 2018). Hence, it will be interesting to further develop and test the potential benefits of our microstructural signature approach in this context.

Second, we apply the t-SNE visualization model to cluster regions according to their microstructural signature values. As expected, we find that similar neuroanatomical areas are adjacent to each other in the t-SNE space. Interestingly, each sub-cortical gray region has a very unique signature that distinguishes it from other brain regions. This microstructural unique signature of subcortical regions echoes earlier work by (Bazin et al., 2020) that used the subcortical unique multi-parametric qMRI to segment those regions. It will be interesting to further expand the t-SNE clustering approach to a wide range of other applications, such as classifying healthy versus diseased states.

Our study has several limitations worth noting. Our sample size in this study is quite small, mostly including young adults(mean age 26.4) and older adults (mean age 66.1) that were used in a previous study (Filo et al., 2019). A larger dataset with broader age ranges is required to verify our findings (For example: (Jansen et al., 2024)). Such a larger dataset may also allow machine learning models to find meaningful insights about the aging effects. Additionally, although our data standardization and median vectorization effectively minimize noise and handle scale differences of the parameters, these methods might also mask some meaningful variations in the data. For example, we find differences in our vector representation if we normalized to whole brain regions or just the cortical and non-cortical regions. For example, the white matter and subcortical inter-regional correlations didn't show a similar pattern of correlation as

the cortical regions and supported only the second hypothesis we tested. Further research needs to be done to investigate whether optimized pre-processing methods are needed for specific brain regions.

We also conducted several experiments that were challenging to interpret. For example, we tried to use clustering methods, such as hierarchical clustering or spectral clustering, to divide the brain regions signatures in each age group, by known functional connectivity or to identify connectivity patterns between the resulting clusters. We couldn't find notable patterns regarding that. However, we did find an interesting result that helped us verify that microstructure signature similarity inside the brain is more correlated in the old group. The hierarchical clustering showed that most of the brain regions in the old groups tend to cluster together.

To conclude, our study provides evidence for increased inter-regional similarity within individuals (particularly in cortical areas) and increased variability across individuals in the aging brain. Our method utilized multi-dimensional normalization and has been proven useful for various tasks such as clustering and classification. These findings contribute to our understanding of normal brain aging and demonstrate the potential of multi-parameter qMRI approaches for investigating brain microstructure. Future research building on this work could significantly advance our knowledge of brain aging.

4 Methods

4.1 Overview

We used qMRI data to test our hypothesis concerning similarities in brain regions during aging. The human dataset used in our study was created by Filo et al. (2019), where the MRI acquisition methods, qMRI parameter estimation, and brain segmentation are thoroughly detailed, we discuss the key findings from there. All of our analyses were conducted using the Python programming language (<https://github.com/python>), and our code is available at: <https://github.com/MezerLab/qMRI-age-similarities>.

4.2 Subjects

We selected 17 young adults (aged 26.4 ± 2.4 years, 9 females, 8 males) and 15 older adults (aged 66.1 ± 5 years, 4 females, 11 males). For each subject, we used seven qMRI maps: R1 ($\frac{1}{T_1}$), T2, MTV, MT, R2* ($\frac{1}{T_{2*}}$), Diffusion FA, and Diffusion MD. All selected subjects are considered healthy.

4.3 MRI acquisition

Data was collected on a 3 T Siemens MAGNETOM Skyra scanner equipped with a 32-channel head receive-only coil at the ELSC neuroimaging unit at the Hebrew University.

For quantitative R1, R2*, and MTV mapping, 3D Spoiled Gradient Echo (SPGR) images were acquired using different flip angles of 4°, 10°, 20°, and 30°. Each image had five echoes spaced with echo times ranging from 3.34 milliseconds (ms) to 14.02 ms, and a repetition time of 19 ms. For T2 mapping, multi-SE images were obtained with ten spin echoes with echo times ranging from 12 ms to 120 ms, and a repetition time of 4.21 seconds. MTsat mapping used SPGR images with an additional MT pulse, a flip angle of 10°, and echo and repetition times of 3.34 ms and 27 ms, respectively. Whole-brain DTI was performed using a diffusion-weighted spin-echo EPI sequence at 1.5 mm resolution, 64 directions, and a diffusion weighting of 2000 seconds per square millimeter, with echo time and repetition time of 95.80 ms and 6000 ms, respectively, a gradient strength of 45 millitesla per meter, a diffusion encoding duration of 32.25 ms, and a diffusion time of 52.02 ms.

4.4 Estimation of qMRI parameters

Whole-brain MTV and R1 maps were computed using the mrQ software (Mezer et al., 2013). T2 maps were computed by implementing the echo-modulation curve (EMC) algorithm (Ben-Eliezer et al., 2015). MTsat maps were computed as described in (Helms et al., 2008). Diffusion analysis was done using the FDT toolbox in FSL (Smith et al., 2004). The R2* was estimated by using SPGR scans with multiple echoes. Fitting was done through the MPM toolbox (Weiskopf et al., 2013).

4.5 Brain segmentation

Whole-brain segmentation was computed automatically using the FreeSurfer segmentation algorithm (Fischl, 2012). Each brain region we used has \sim 6400 voxels, on average. FreeSurfer allocates each voxel to its corresponding brain region by combining intensity-based classification, probabilistic atlases - such as Desikan-Killiany Atlas (Desikan et al., 2006), and anatomical constraints such as location, shape, and curvature. After aligning the MRI scan to a reference atlas, the software analyzes the voxel's intensity to determine the tissue type and uses spatial priors from the atlas to estimate the likelihood of the voxel belonging to a specific region.

4.6 Dataset construction

In Section 3.1 we elaborated on our novel method to use the data for our analysis, and now we discuss its technical properties.

To extract the 3D brain qMRI maps and segmentation maps for each subject, we used nibabel package (<https://github.com/nipy/nibabel>). The regions were divided to fit the segmentation maps using NumPy (Harris et al., 2020) methods.

We standardized voxel values within the brain regions using the z-score method ($z = \frac{x - \mu}{\sigma}$) implemented in the SciPy library Virtanen et al. (2020). Initially, we combined all neuroanatomical areas (cortical, white matter, and subcortical) for standardization, but this resulted in a non-normal distribution that persisted even after standardization. To address this, we standardized each neuroanatomical area separately, as they each followed a normal distribution independently, leading to a normalized distribution for the combined regions.

The median values were calculated using NumPy (Harris et al., 2020) and the final resulting data matrix of each subject was stored in pandas DataFrame (McKinney et al., 2010).

4.7 Outliers handling

Originally, the dataset contained 37 subjects. We removed subjects identified as noisy outliers using an interquartile range (IQR) method. For each parameter, we calculated the first quartile (Q1) and the third quartile (Q3) values. Outliers were identified as those data points falling on average, below Q1 minus a threshold (multiplied by the IQR), or above Q3 plus the same threshold. We applied the same method for the brain regions, to remove noisy regions. We ended up with 32 subjects in total and 128 brain regions for each one.

4.8 Correlations analysis

First, the hierarchical clustering used as a baseline for determining the order of the ROIs in the correlation matrices was based on the average linkage method, calculated as:

$$d(u, v) = \frac{1}{|u| \cdot |v|} \sum_{i \in u} \sum_{j \in v} d(i, j),$$

where the distance metric $d(i, j)$ represents the cosine distance between points i and j . Cosine distance is defined as:

$$d(i, j) = 1 - \frac{\mathbf{x}_i \cdot \mathbf{x}_j}{\|\mathbf{x}_i\| \|\mathbf{x}_j\|},$$

where \mathbf{x}_i and \mathbf{x}_j are the vectors representing the ROIs. This distance metric was used to capture the similarity between different ROIs based on their angular separation, ensuring the clustering reflects both magnitude and directional information in the data. This approach was implemented using the Scipy library (Virtanen et al., 2020).

Then, the Pearson correlation coefficient (see below) between each two ROIs median vectors was calculated to achieve a 128×128 correlation matrix. The correlation was computed using the built-in pandas DataFrame (McKinney et al., 2010) correlation method.

$$r = \frac{\sum (x_i - \bar{x})(y_i - \bar{y})}{\sqrt{\sum (x_i - \bar{x})^2 \sum (y_i - \bar{y})^2}}.$$

4.9 Statistical significance

Through our analyses, we aimed to determine whether there were significant differences between the findings of the young and old groups. To achieve this, we used an independent two-sample t-test (`ttest_ind` method) from the Scipy (Virtanen et al., 2020) library.

4.10 Dimensionality reduction using t-SNE

For dimensionality reduction, we employed a using t-distributed stochastic neighbor embedding (t-SNE) model implemented by scikit-learn (Pedregosa et al., 2011). We used the default hyperparameters for the t-SNE model, except for setting the number of components to 2 (for 2-D visualization) and adjusting the perplexity to 100, which was selected after testing several values.

4.11 XGboost model for Binary Classification

We used the default XGboost (Chen and Guestrin, 2016) classifier, for our ROIs binary classification of age group. We trained Each of the models using this classifier's built-in training method.

References

- Abraham, A., Pedregosa, F., Eickenberg, M., Gervais, P., Mueller, A., Kos-saifi, J., Gramfort, A., Thirion, B., and Varoquaux, G. (2014). Machine learning for neuroimaging with scikit-learn. *Frontiers in neuroinformatics*, 8:71792.
- Anderson, A. W. (2005). Measurement of fiber orientation distributions using high angular resolution diffusion imaging. *Magnetic Resonance in Medicine: An Official Journal of the International Society for Magnetic Resonance in Medicine*, 54(5):1194–1206.
- Aycheh, H. M., Seong, J.-K., Shin, J.-H., Na, D. L., Kang, B., Seo, S. W., and Sohn, K.-A. (2018). Biological brain age prediction using cortical thickness data: a large scale cohort study. *Frontiers in aging neuroscience*, 10:252.
- Baecker, L., Garcia-Dias, R., Vieira, S., Scarpazza, C., and Mechelli, A. (2021). Machine learning for brain age prediction: Introduction to methods and clinical applications. *EBioMedicine*, 72.
- Bauer, S., Wiest, R., Nolte, L.-P., and Reyes, M. (2013). A survey of mri-based medical image analysis for brain tumor studies. *Physics in Medicine & Biology*, 58(13):R97.
- Bazin, P.-L., Alkemade, A., Mulder, M. J., Henry, A. G., and Forstmann, B. U. (2020). Multi-contrast anatomical subcortical structures parcellation. *Elife*, 9:e59430.
- Ben-Eliezer, N., Sodickson, D. K., and Block, K. T. (2015). Rapid and accurate t2 mapping from multi-spin-echo data using bloch-simulation-based reconstruction. *Magnetic resonance in medicine*, 73(2):809–817.

- Burzynska, A. Z., Nagel, I. E., Preuschhof, C., Gluth, S., Bäckman, L., Li, S.-C., Lindenberger, U., and Heckeren, H. R. (2012). Cortical thickness is linked to executive functioning in adulthood and aging. *Human brain mapping*, 33(7):1607–1620.
- Callaghan, M. F., Freund, P., Draganski, B., Anderson, E., Cappelletti, M., Chowdhury, R., Diedrichsen, J., FitzGerald, T. H., Smittenaar, P., Helms, G., et al. (2014). Widespread age-related differences in the human brain microstructure revealed by quantitative magnetic resonance imaging. *Neurobiology of aging*, 35(8):1862–1872.
- Carey, D., Caprini, F., Allen, M., Lutti, A., Weiskopf, N., Rees, G., Callaghan, M. F., and Dick, F. (2018). Quantitative mri provides markers of intra-, inter-regional, and age-related differences in young adult cortical microstructure. *Neuroimage*, 182:429–440.
- Chen, T. and Guestrin, C. (2016). Xgboost: A scalable tree boosting system. In *Proceedings of the 22nd ACM SIGKDD international conference on knowledge discovery and data mining*, pages 785–794.
- Chougar, L., Pyatigorskaya, N., Degos, B., Grabli, D., and Lehéricy, S. (2020). The role of magnetic resonance imaging for the diagnosis of atypical parkinsonism. *Frontiers in Neurology*, 11:665.
- Desikan, R. S., Ségonne, F., Fischl, B., Quinn, B. T., Dickerson, B. C., Blacker, D., Buckner, R. L., Dale, A. M., Maguire, R. P., Hyman, B. T., et al. (2006). An automated labeling system for subdividing the human cerebral cortex on mri scans into gyral based regions of interest. *Neuroimage*, 31(3):968–980.
- Dugger, B. N. and Dickson, D. W. (2017). Pathology of neurodegenerative diseases. *Cold Spring Harbor perspectives in biology*, 9(7):a028035.
- Edwards, L. J., Kirilina, E., Mohammadi, S., and Weiskopf, N. (2018). Microstructural imaging of human neocortex in vivo. *Neuroimage*, 182:184–206.
- Erickson, K. I., Voss, M. W., Prakash, R. S., Basak, C., Szabo, A., Chaddock, L., Kim, J. S., Heo, S., Alves, H., White, S. M., et al. (2011). Exercise training increases size of hippocampus and improves memory. *Proceedings of the national academy of sciences*, 108(7):3017–3022.

- Filo, S., Shtangel, O., Salamon, N., Kol, A., Weisinger, B., Shifman, S., and Mezer, A. A. (2019). Disentangling molecular alterations from water-content changes in the aging human brain using quantitative mri. *Nature communications*, 10(1):3403.
- Fischl, B. (2012). Freesurfer. *Neuroimage*, 62(2):774–781.
- Fjell, A. M. and Walhovd, K. B. (2010). Structural brain changes in aging: courses, causes and cognitive consequences. *Reviews in the Neurosciences*, 21(3):187–222.
- Frisoni, G. B., Fox, N. C., Jack Jr, C. R., Scheltens, P., and Thompson, P. M. (2010). The clinical use of structural mri in alzheimer disease. *Nature reviews neurology*, 6(2):67–77.
- Gracien, R.-M., Nürnberg, L., Hok, P., Hof, S.-M., Reitz, S. C., Rüb, U., Steinmetz, H., Hilker-Roggendorf, R., Klein, J. C., Deichmann, R., et al. (2017). Evaluation of brain ageing: a quantitative longitudinal mri study over 7 years. *European radiology*, 27:1568–1576.
- Guo, D., Fridriksson, J., Fillmore, P., Rorden, C., Yu, H., Zheng, K., and Wang, S. (2015). Automated lesion detection on mri scans using combined unsupervised and supervised methods. *BMC medical imaging*, 15:1–21.
- Harman, D. (1981). The aging process. *Proceedings of the National Academy of Sciences*, 78(11):7124–7128.
- Harris, C. R., Millman, K. J., van der Walt, S. J., Gommers, R., Virtanen, P., Cournapeau, D., Wieser, E., Taylor, J., Berg, S., Smith, N. J., Kern, R., Picus, M., Hoyer, S., van Kerkwijk, M. H., Brett, M., Haldane, A., Fernández del Río, J., Wiebe, M., Peterson, P., Gérard-Marchant, P., Sheppard, K., Reddy, T., Weckesser, W., Abbasi, H., Gohlke, C., and Oliphant, T. E. (2020). Array programming with numpy. *Nature*, 585(7825):357–362.
- Hashemi, R. H., Bradley, W. G., and Lisanti, C. J. (2012). *MRI: the basics: The Basics*. Lippincott Williams & Wilkins.
- Helms, G., Dathe, H., Kallenberg, K., and Dechent, P. (2008). High-resolution maps of magnetization transfer with inherent correction for rf inhomogeneity and t1 relaxation obtained from 3d flash mri. *Magnetic Resonance in Medicine: An Official Journal of the International Society for Magnetic Resonance in Medicine*, 60(6):1396–1407.

- Hou, Y., Dan, X., Babbar, M., Wei, Y., Hasselbalch, S. G., Croteau, D. L., and Bohr, V. A. (2019). Ageing as a risk factor for neurodegenerative disease. *Nature Reviews Neurology*, 15(10):565–581.
- Hung, C.-W., Chen, Y.-C., Hsieh, W.-L., Chiou, S.-H., and Kao, C.-L. (2010). Ageing and neurodegenerative diseases. *Ageing research reviews*, 9:S36–S46.
- Izgi, H., Han, D., İşıldak, U., Huang, S., Kocabiyik, E., Khaitovich, P. E., Somel, M., and Dönertaş, H. M. (2022). Inter-tissue convergence of gene expression during ageing suggests age-related loss of tissue and cellular identity. *eLife*, 11.
- Jansen, M. G., Zwiers, M. P., Marques, J. P., Chan, K.-S., Amelink, J. S., Altgassen, M., Oosterman, J. M., and Norris, D. G. (2024). The advanced brain imaging on ageing and memory (abrim) data collection: Study design, data processing, and rationale. *PLOS ONE*, 19(6):e0306006.
- Kremen, W. S., Prom-Wormley, E., Panizzon, M. S., Eyler, L. T., Fischl, B., Neale, M. C., Franz, C. E., Lyons, M. J., Pacheco, J., Perry, M. E., et al. (2010). Genetic and environmental influences on the size of specific brain regions in midlife: the veterans mri study. *Neuroimage*, 49(2):1213–1223.
- Lee, J., Burkett, B. J., Min, H.-K., Senjem, M. L., Lundt, E. S., Botha, H., Graff-Radford, J., Barnard, L. R., Gunter, J. L., Schwarz, C. G., et al. (2022). Deep learning-based brain age prediction in normal aging and dementia. *Nature Aging*, 2(5):412–424.
- Leung, D., Han, X., Mikkelsen, T., and Nabors, L. B. (2014). Role of mri in primary brain tumor evaluation. *Journal of the National Comprehensive Cancer Network*, 12(11):1561–1568.
- Lockhart, S. N. and DeCarli, C. (2014). Structural imaging measures of brain aging. *Neuropsychology review*, 24:271–289.
- McKinney, W. et al. (2010). Data structures for statistical computing in python. In *Proceedings of the 9th Python in Science Conference*, volume 445, pages 51–56. Austin, TX.
- Mezer, A., Yeatman, J. D., Stikov, N., Kay, K. N., Cho, N.-J., Dougherty, R. F., Perry, M. L., Parvizi, J., Hua, L. H., Butts-Pauly, K., et al. (2013). Quantifying the local tissue volume and composition in individual

- brains with magnetic resonance imaging. *Nature medicine*, 19(12):1667–1672.
- Morrow, M., Waters, J., and Morris, E. (2011). MRI for breast cancer screening, diagnosis, and treatment. *The Lancet*, 378(9805):1804–1811.
- Muller, M., Sigurdsson, S., Kjartansson, O., Aspelund, T., Lopez, O. L., Jonnson, P. V., Harris, T. B., Van Buchem, M., Gudnason, V., Launer, L. J., et al. (2014). Joint effect of mid-and late-life blood pressure on the brain: the ages-reykjavik study. *Neurology*, 82(24):2187–2195.
- Nadig, A., Seidlitz, J., McDermott, C. L., Liu, S., Bethlehem, R., Moore, T. M., Mallard, T. T., Clasen, L. S., Blumenthal, J. D., Lalonde, F., et al. (2021). Morphological integration of the human brain across adolescence and adulthood. *Proceedings of the National Academy of Sciences*, 118(14):e2023860118.
- Paquola, C., Bethlehem, R. A., Seidlitz, J., Wagstyl, K., Romero-Garcia, R., Whitaker, K. J., Vos de Wael, R., Williams, G. B., Consortium, N., Vértes, P. E., et al. (2019a). Shifts in myeloarchitecture characterise adolescent development of cortical gradients. *elife*, 8:e50482.
- Paquola, C., Vos De Wael, R., Wagstyl, K., Bethlehem, R. A., Hong, S.-J., Seidlitz, J., Bullmore, E. T., Evans, A. C., Misic, B., Margulies, D. S., et al. (2019b). Microstructural and functional gradients are increasingly dissociated in transmodal cortices. *PLoS biology*, 17(5):e3000284.
- Pedregosa, F., Varoquaux, G., Gramfort, A., Michel, V., Thirion, B., Grisel, O., Blondel, M., Prettenhofer, P., Weiss, R., Dubourg, V., et al. (2011). Scikit-learn: Machine learning in python. *the Journal of machine Learning research*, 12:2825–2830.
- Peters, R. (2006). Ageing and the brain: This article is part of a series on ageing edited by professor chris bulpitt. *Postgraduate medical journal*, 82(964):84–88.
- Plewes, D. B. and Kucharczyk, W. (2012). Physics of mri: a primer. *Journal of magnetic resonance imaging*, 35(5):1038–1054.
- Raz, N., Lindenberger, U., Rodriguez, K. M., Kennedy, K. M., Head, D., Williamson, A., Dahle, C., Gerstorf, D., and Acker, J. D. (2005). Regional brain changes in aging healthy adults: general trends, individual differences and modifiers. *Cerebral cortex*, 15(11):1676–1689.

- Smith, S. M., Jenkinson, M., Woolrich, M. W., Beckmann, C. F., Behrens, T. E., Johansen-Berg, H., Bannister, P. R., De Luca, M., Drobnjak, I., Flitney, D. E., et al. (2004). Advances in functional and structural mr image analysis and implementation as fsl. *Neuroimage*, 23:S208–S219.
- Sowell, E. R., Thompson, P. M., and Toga, A. W. (2004). Mapping changes in the human cortex throughout the span of life. *The Neuroscientist*, 10(4):372–392.
- Thambisetty, M., Wan, J., Carass, A., An, Y., Prince, J. L., and Resnick, S. M. (2010). Longitudinal changes in cortical thickness associated with normal aging. *Neuroimage*, 52(4):1215–1223.
- Valls-Pedret, C., Sala-Vila, A., Serra-Mir, M., Corella, D., De la Torre, R., Martínez-González, M. Á., Martínez-Lapiscina, E. H., Fitó, M., Pérez-Heras, A., Salas-Salvadó, J., et al. (2015). Mediterranean diet and age-related cognitive decline: a randomized clinical trial. *JAMA internal medicine*, 175(7):1094–1103.
- Vernooij, M. W., Ikram, M. A., Tanghe, H. L., Vincent, A. J., Hofman, A., Krestin, G. P., Niessen, W. J., Breteler, M. M., and van der Lugt, A. (2007). Incidental findings on brain mri in the general population. *New England Journal of Medicine*, 357(18):1821–1828.
- Virtanen, P., Gommers, R., Oliphant, T. E., Haberland, M., Reddy, T., Cournapeau, D., Burovski, E., Peterson, P., Weckesser, W., Bright, J., et al. (2020). Scipy 1.0: fundamental algorithms for scientific computing in python. *Nature methods*, 17(3):261–272.
- Weiskopf, N., Suckling, J., Williams, G., Correia, M. M., Inkster, B., Tait, R., Ooi, C., Bullmore, E. T., and Lutti, A. (2013). Quantitative multi-parameter mapping of r1, pd*, mt, and r2* at 3t: a multi-center validation. *Frontiers in neuroscience*, 7:95.
- Wrigglesworth, J., Ryan, J., Ward, P. G., Woods, R. L., Storey, E., Egan, G. F., Murray, A., Espinoza, S. E., Shah, R. C., Trevaks, R. E., et al. (2023). Health-related heterogeneity in brain aging and associations with longitudinal change in cognitive function. *Frontiers in Aging Neuroscience*, 14:1063721.
- Wu, J., Li, Y., and Ma, Y. (2021). Comparison of xgboost and the neural network model on the class-balanced datasets. In *2021 IEEE 3rd international conference on frontiers technology of information and computer (ICFTIC)*, pages 457–461. IEEE.

Yeatman, J. D., Wandell, B. A., and Mezer, A. A. (2014). Lifespan maturation and degeneration of human brain white matter. *Nature communications*, 5(1):4932.

Zhang, S., Xu, S., Tan, L., Wang, H., and Meng, J. (2021). Stroke lesion detection and analysis in mri images based on deep learning. *Journal of Healthcare Engineering*, 2021(1):5524769.